Enhanced creation of dispersive monolayer phonons in Xe/Pt(111) by inelastic helium atom scattering at low energies

Hansen, Flemming Yssing; Bruch, Ludwig Walter

Published in:
Journal of Chemical Physics

Link to article, DOI:
10.1063/1.2786990

Publication date:
2007

Document Version
Publisher's PDF, also known as Version of record

Enhanced creation of dispersive monolayer phonons in Xe/Pt(111) by inelastic helium atom scattering at low energies

F. Y. Hansen[a)]
Department of Chemistry, Technical University of Denmark, IK-207-DTU, DK-2800 Lyngby, Denmark

L. W. Bruch
Department of Physics, University of Wisconsin-Madison, Madison, Wisconsin 53706, USA

(Received 28 June 2007; accepted 28 August 2007; published online 28 November 2007)

Conditions likely to lead to enhanced inelastic atomic scattering that creates shear horizontal (SH) and longitudinal acoustic (LA) monolayer phonons are identified, specifically examining the inelastic scattering of ^{4}He atoms by a monolayer solid of Xe/Pt(111) at incident energies of 2–25 meV. There is strong inelastic scattering for both dispersive phonon branches (SH and LA) of the monolayer at incident energies below 8 meV. Several improvements enable more complete wave packet calculations of the inelastic scattering than in previous work. Long propagation times are made feasible by adding an absorbing potential at large distance. The times now extend to beyond 100 ps and enable a clarification of processes involving transient trapping of the He atoms. The wave packet is made more monochromatic by significantly increasing the spatial width of the initial Gaussian shape. The narrower energy distribution in the incident beam then enables a demonstration of strong energy dependence of the scattering over a scale of less than 0.3 meV. © *2007 American Institute of Physics*. [DOI: 10.1063/1.2786990]

I. INTRODUCTION

Inelastic scattering from a nearly harmonic lattice and its low-temperature thermodynamics are expressed in terms of the properties of the excitation quanta, the phonons, of the normal modes of vibration. Thus, determining the phonon dispersion relations is basic to a fundamental characterization of the response of the lattice.[1,2] It is now feasible[3–8] to do such measurements on single monolayer solid domains using low energy inelastic helium atom scattering (HAS). An unanticipated result of the experiments was that all branches of the dispersion relations were accessed for wave vectors near high-symmetry azimuths in the first Brillouin zone.[6] In a previous paper,[9] denoted as Paper I, we demonstrated that the anomalous excitation of shear horizontal (SH) phonon modes by HAS from a physically adsorbed monolayer can be understood using a strong coupling inelastic scattering theory and known atomic interactions. The basic calculation was to generate the time-dependent solution for wave packet scattering, with the inelastic processes treated in the one-phonon creation approximation. The apparent violation of basic polarization selection rules[2] can be an intrinsic effect arising from a small misalignment, 1°–2°, of the scattering plane relative to high-symmetry axes of the monolayer solid lattice. Such small misalignments are common in experiments on physisorbed monolayers, but they had been assumed to have no serious consequences.[10]

In the present paper, we attempt to provide some guidance for future experiments by identifying conditions that enhance the strength of the inelastic scattering for creating dispersive phonons, especially by treating lower incident energies. Also we determine the time scales for transient trapping of the incident atom that has been noted in previous calculations[9,11–13] and which extends over times of 20–80 ps in several cases. Our results are for the scattering of ^{4}He by a Xe/Pt(111) monolayer at incident energies of 2–25 meV and the parameter space has been reduced by specifying that the geometry is such that the incident angle leads to an inelastic outgoing wave at an angle corresponding to the scan curve geometry of the principal experiments[6,8] (Fig. 1). The strong inelastic scattering and the long transients in the elastic scattering both are associated with strong coupling effects in low energy scattering, but they do not coincide with resonance conditions, e.g., they do not seem to be directly associated with selective adsorption resonances.[14] Quantum reflection is a phenomenon at far lower energy[15] than treated here.

We find that the inelastic scattering generally is enhanced as the incident wave packet energy E_i decreases from 8 to 4 meV, i.e., still about 2 meV above the threshold for most of the cases treated here. We also calculate the response as a function of energy E_i near 8 meV, with energy increments of 0.15 meV, and demonstrate that there are large variations in the scattered strengths for energy variations of order 0.3 meV. Together these results suggest that a fruitful line for experiments will be to explore scattering energies in the range 4–8 meV with a resolution of better than 0.3 meV.

There are several improvements in the methodology relative to Paper I. (1) The calculations are extended to much longer propagation times to ensure that the scattering event is completed. The packet propagates on a bounded space grid, so some of the packet reaches the far boundary while some is still near the monolayer. Therefore, an absorbing potential[16] is added at large perpendicular distance from the monolayer

[a)]Electronic mail: flemming@kemi.dtu.dk

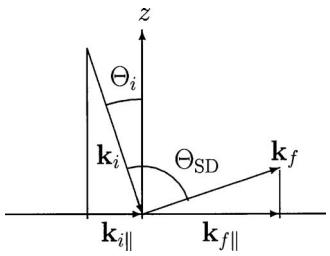

FIG. 1. Scan curve geometry used in many experiments (Ref. 8). The angle of incidence Θ_i is set by the requirement that the angle between the incident wave vector $\mathbf{k}_i$ and the final wave vector $\mathbf{k}_f$ for a specified phonon creation event is kept fixed, $\Theta_{SD}=95.8°$ in one set of experiments (Ref. 6) and the present calculations. The magnitude k_f is set by energy conservation and Θ_i is chosen to make $\mathbf{k}_{i\|}-\mathbf{k}_{f\|}=\mathbf{q}$, corresponding to the specular channel ($\mathbf{g}=0$). The plane of incidence is specified by $\mathbf{k}_i$ and $\hat{z}$.

target and the flux into the absorber and the total scattering are calculated for each channel (Appendix A). This extension is needed also because there are many instances where scattering components with nonzero reciprocal lattice vector transfers $\mathbf{g}\neq 0$ have larger perpendicular velocity than the $\mathbf{g}=0$ components that are mostly accessed in experiments with scan curve constraints. (2) Similarly, the lateral vibration contributions to the Debye-Waller factor,[17,18] which were small for $\mathbf{g}=0$, become appreciable for the large $|\mathbf{g}|$ components and modify the distribution of scattered strengths. (3) For low incident energies, $E_i<8$ meV, the magnitude of the attractive potential energy between the atom and the monolayer is comparable to E_i and we use the Beeby correction[19–21] to estimate the effect of this "inner potential." (4) The calculations give a large amount of information on the scattering and we introduce statistical characterizations[22,23] to get an overview of the distribution of scattered strengths over channels (Appendix B). (5) We make more thorough tests of parameters in the numerical implementation to assure that the results are evaluated to significantly better than 10% in precision (Appendix C).

The organization of this paper is as follows: Section II summarizes the formulation of the scattering theory and its implementation. Section III presents an overview of the energy dependence of the inelastic scattering to create dispersive phonons. Analysis of scattering events with significant transiently trapped intensity is presented in Sec. IV. Final remarks are given in Sec. V. Additional details on the theory and methods are presented in three appendixes.

II. THEORY

A. Notation and definitions

The mass of an atom in the incident beam (^{4}He in this paper) is denoted m and of an atom in the target monolayer [Xe/Pt(111)] is denoted M. The monolayer is a regular planar triangular lattice incommensurate with the substrate and with one atom per unit cell and nearest-neighbor spacing L_{nn}. Then, a monolayer of N atoms has N wave vectors in the first Brillouin zone. The reciprocal lattice is spanned by primitive vectors $\mathbf{g}_1$ and $\mathbf{g}_2$ of length $g_0=4\pi/(L_{nn}\sqrt{3})$ and at an angle 120° to each other.

There are three branches to the dispersion relation, denoted S for the polarization primarily perpendicular ($\hat{z}$) to the monolayer plane and SH (shear horizontal) and LA (longitudinal acoustic) for the branches primarily in the plane and which have the pure designated polarizations for wave vectors along high-symmetry azimuths of the monolayer. $\omega(\mathbf{q},\lambda)$ is the frequency of the normal mode with wave vector $\mathbf{q}$ in the branch λ and $\hat{\mathbf{e}}(\mathbf{q},\lambda)$ is the normalized polarization vector. Vibrations perpendicular to the monolayer plane (S mode) decouple from those in the plane and are nearly dispersionless.

Let the incident probe atom (^{4}He) have wave vector $\mathbf{k}_i=(\mathbf{k}_{i\|},k_{iz})$ and energy $\epsilon_i=\hbar^2k_i^2/2m$. The final energy is $\epsilon_f=\epsilon_i-\hbar\omega(\mathbf{q},\lambda)$ for inelastic scattering creating a $(\mathbf{q},\lambda)$ phonon. The channels are labeled by the parallel wave vectors $\mathbf{k}_\|=\mathbf{k}_{i\|}+\mathbf{g}-\mathbf{q}$, where $\mathbf{g}=i\mathbf{g}_1+j\mathbf{g}_2$ with i and j integers. The corresponding free-atom kinetic energy is $\epsilon_\|=\hbar^2k_\|^2/2m$ and channels are defined to be closed or open according to whether the sign of $\Delta=\epsilon_\|-\epsilon_f$ is positive or negative. For diffraction (elastic scattering), the $q=\omega=0$ case of these definitions is used. The $\mathbf{g}=0$ channel is termed the *specular* channel.

Depending on the parameters, a channel with a given $\mathbf{g}$ can be open or closed for one or both elastic and inelastic scattering. As a scale for discussing the closed channels,[24] we use the bound state energy levels ϵ_α of the atom in the laterally averaged potential $V_0(z)$ from the monolayer. Table I gives the properties of these states. For $\mathbf{q}=0$, the condition $\Delta=|\epsilon_\alpha|$ is an approximation to selective adsorption resonances which neglects band structure effects.[25,26]

Throughout the paper, energies are given in meV and K, lengths in Å, and wave numbers in Å^{-1}.

TABLE I. Calculated energy, average distance $\langle z\rangle$ from the surface, the standard deviation σ_z of z, and the inner and outer classical turning points for the stationary states of a ^{4}He atom in the laterally averaged potential, $V_0(z)$, from the Xe/Pt(111) monolayer with $L_{nn}=4.33$ Å. The minimum of V_0 is −7.763 meV at $z=3.25$ Å. The interaction model is specified in Sec. II F. Energies are in meV and lengths in Å.

				Classical turning points (Å)	
State	Energy (meV)	$\langle z\rangle$ (Å)	σ_z (Å)	Inner	Outer
1	−5.434	3.79	0.38	3.19	4.19
2	−2.365	4.57	0.79	3.07	5.29
3	−0.863	5.92	1.20	3.03	6.98
4	−0.259	8.37	1.93	3.02	10.00
5	−0.059	13.19	3.36	3.01	15.92

TABLE II. Phonon energies in meV as a function of wave number q in Å^{-1} along an azimuth at 2.6° to the ΓM azimuth of a xenon monolayer with L_{nn}=4.33 Å, calculated for the HFD-B2 potential with McLachlan substrate-mediated interactions as in Paper I. The S-mode energy is $\hbar\omega_{\perp}$=3.5 meV.

	$\hbar\omega(q)$ (meV)	
q (Å^{-1})	SH	LA
0.125	0.636	1.12
0.250	1.24	2.18
0.500	2.21	3.91

B. Inelastic scattering theory: One-phonon approximation

We refer to our previous paper,[9] denoted as Paper I, for a full description of the theory but repeat a few central parts here. New features of the calculations are described in Secs. II C–II E.

The scattering target is a monolayer solid of (Xe) atoms in the xy plane, supported by a static substrate, and the probe (^{4}He) atom approaches from the $z>0$ space. The initial state of the incident atom is a wave packet formed from the product of a plane wave function for the lateral motion ($\mathbf{k}_{i\|}$) parallel to the surface and a Gaussian for the spatial distribution along $\hat{z}$ [Eq. (C1)]. For a large Gaussian width, the incident wave is rather monochromatic; i.e., the spread in the z component k_{iz} of the incident wave vector $\mathbf{k}_i$ is small. In most of the present work, the corresponding energy widths are on the scale of 0.3 meV and are close to the overall energy resolution in recent low energy HAS experiments.[8]

The potential energy of interaction $V_s(\mathbf{r},z)$ of the probe atom with the static monolayer is decomposed with the Steele series[17]

$$V_s(\mathbf{r},z) = V_0(z) + \sum_{\mathbf{g}} V(\mathbf{g},z)\exp(i\mathbf{g}\cdot\mathbf{r}), \tag{1}$$

where $\mathbf{g}$ are the monolayer reciprocal lattice vectors.

The Schrödinger equation for the channel amplitudes in the elastically scattered (diffracted) wave function Ψ_0 is

$$i\hbar\frac{\partial\psi_{\mathbf{g}}(z,t)}{\partial t} = \frac{\hbar^2}{2m}\left[(\mathbf{g}+\mathbf{k}_{i\|})^2 - \frac{\partial^2}{\partial z^2}\right]\psi_{\mathbf{g}}(z,t) + \sum_{\mathbf{g}'} V(\mathbf{g}-\mathbf{g}',z)\psi_{\mathbf{g}'}(z,t). \tag{2}$$

The final term on the right-hand side of the equation couples the channels with potential energy coefficients $V(\mathbf{g}-\mathbf{g}',z)$.

The Schrödinger equation for the channel amplitudes in the one-phonon inelastic wave function Ψ_1 is

TABLE III. Summary of angles of incidence Θ_i and asymptotic decay times τ for the elastic (diffracted) wave function Ψ_0. The plane of incidence is at 2.6° to the ΓM axis of the Xe/Pt(111) monolayer and the phonon wave vectors $\mathbf{q}$ are along this azimuth, as in Paper I. For each case, Θ_i is given as a second line below the τ_1 and the columns are ordered to make a monotonic variation of Θ_i as one goes across a row. Calculations of Θ_i are for scan curve conditions at Θ_{SD}=95.8° and the specified inelastic scattering mode and wave vector. Energies E_i are in meV, wave numbers q in Å^{-1}, and times τ in ps. The … denote cases where a second decay time τ_2 could not be determined.

	τ_1 (ps)				τ_2 (ps)			
q (Å^{-1})	−0.125	−0.125	−0.25	−0.25	−0.125	−0.125	−0.25	−0.25
E_i (meV)	SH	LA	SH	LA	SH	LA	SH	LA
2.0	2.7 38.98°		5.2 26.69°		34.0		58.5	
2.5		5.9 35.93°		≈10 13.7°		…		≈130
4.0	3.7 43.20°	4.3 40.68°	8.9 37.85°	12.0 31.28°	21.3	20.5	33.5	82.3
5.0	1.9 44.00°	5.4 42.10°	14.8 39.71°	14.8 35.09°	11.3	21.7	66.8	…
6.0	2.4 44.54°	3.0 43.01°	18.9 40.92°	5.5 37.36°	10.9	14.5	…	29.1
8.2	2.9 45.25°	4.0 44.20°	5.4 42.50°	8.5 40.15°	17.2	20.3	…	…
16.6	2.1 46.34°	4.4 45.84°	12.3 44.74°	2.0 43.72°	13.6	14.4	…	14.9
26.5	1.9 46.77°	2.1 46.47°	3.6 45.63°	3.2 45.02°	6.5	7.3	…	9.5

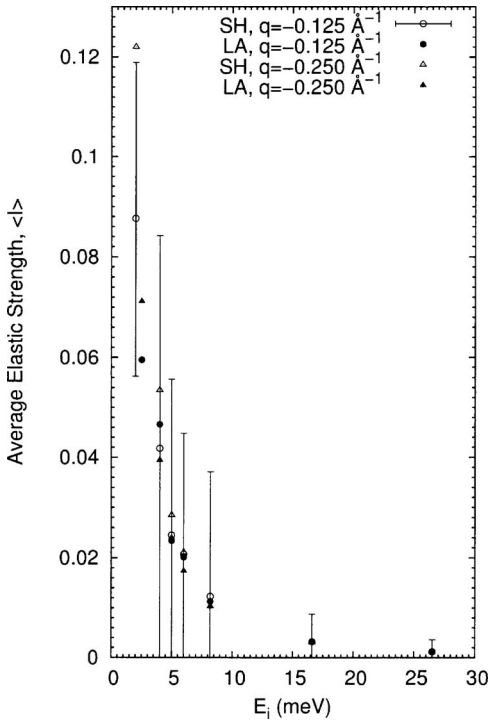

FIG. 2. The average elastic strength $\langle I\rangle=\bar{I}_{\mathrm{el}}$, with the Debye-Waller factor at 50 K included, in an open channel as a function of incident energy E_i for four scan curve conditions, combining two wave vectors $\mathbf{q}$ and two polarizations SH and LA. The incident angles Θ_i for the different conditions are listed in Table III. The plane of incidence is at 2.6° to the ΓM axis of the Xe/Pt(111) monolayer and $\mathbf{q}$ lies in this plane (see Ref. 9). The error bars denote the standard deviation of the averages for the SH series at $q=-0.125$ Å^{-1} (precision of calculation for a given channel is better than 1%); those for the other three cases are similar but omitted in the plot for clarity. Energies E_i are in meV and wave numbers q in Å^{-1}. Open symbols denote SH polarization, whereas filled symbols denote LA polarization.

$$
\begin{aligned}
i\hbar\frac{\partial S_{\mathbf{q},\lambda}(\mathbf{g},z,t)}{\partial t}
&= \left(\frac{\hbar^2}{2m}\left[(\mathbf{k}_{i\|}-\mathbf{q}+\mathbf{g})^2-\frac{\partial^2}{\partial z^2}\right]+\hbar\omega(\mathbf{q},\lambda)\right)S_{\mathbf{q},\lambda}(\mathbf{g},z,t)\\
&\quad+\sum_{\mathbf{g}'}V(\mathbf{g}-\mathbf{g}',z)S_{\mathbf{q},\lambda}(\mathbf{g}',z,t)\\
&\quad+\sum_{\mathbf{g}'}C_\lambda(\mathbf{g}-\mathbf{g}'-\mathbf{q},z)\psi_{\mathbf{g}'}(z,t). \qquad (3)
\end{aligned}
$$

The first terms on the right-hand side of Eq. (3) govern the coupled-channel propagation of Ψ_1 in analogy to Eq. (2) for Ψ_0. Finally, the source term for the inelastic channels driven by the diffraction channels has coefficients C_λ given by

$$
\begin{aligned}
C_\lambda(\mathbf{g}-\mathbf{q},z) &= -\sqrt{\hbar/(2MN\omega(\mathbf{q},\lambda))}\times\hat{\mathbf{e}}(\mathbf{q},\lambda)\\
&\quad\cdot[i(\mathbf{g}-\mathbf{q})V(\mathbf{g}-\mathbf{q},z)+\hat{\mathbf{z}}(dV(\mathbf{g}-\mathbf{q})/dz)]. \qquad (4)
\end{aligned}
$$

The magnitudes of the coupling coefficients $V(\mathbf{g},z)$ in Eq. (2) and $V(\mathbf{g}+\mathbf{q},z)$ in Eq. (4) decrease rapidly for increasing magnitude of $\mathbf{g}$ and z. The calculations were done using $N=1$ in the prefactor for C_λ. We find that six shells of reciprocal lattice vectors suffice in Eq. (1) for the relatively corrugated xenon monolayer.

C. Absorbing potential

In order to allow for the time evolution of an atom transiently trapped in a bound state of $V_0(z)$, it is necessary to propagate the system for long times, usually to at least 50 ps and even longer for low incident atom energy. Then, artifacts might arise from components of the outgoing wave functions that reflect from the far end of the spatial grid at $z_{\max}$. To eliminate the reflection, we add an absorbing potential $-iU$ of a form treated by Vibók and Balint-Kurti.[16] In the notation of Appendix A, the function U is

$$
U(z)=A\exp[-2L/(z-z_U)],\quad z_U<z<z_U+L, \qquad (5)
$$

and is zero otherwise. Ordinarily, we take $z_U=z_{\max}-L$, so U only acts near the far end of the grid. The values of A and L depend on the incident energy and, based on the optimization study of Vibók and Balint-Kurti,[16] we use $L=8\pi/|k_{iz}|$ and $A=24.24(\hbar^2k_{iz}^2/2m)$. These are set to give very small total reflected and transmitted (i.e., nonabsorbed) intensities for the specular elastic channel and, in our experience, these intensities are very small in other channels too.

The time propagation scheme for the calculations which include U is modified[27] as described in Appendix A.

D. Debye-Waller factor

We make *ad hoc* estimates of the effect of thermally excited monolayer vibrations on scattered strengths using the harmonic approximation to the Debye-Waller factor F_{DW}. The effect of the complex platinum surface dynamics[28] on the incommensurate monolayer is omitted; some model calculations[29] for dynamically coupled higher-order commensurate xenon-platinum systems had found only small shifts in the xenon density of states (mean-square displacements were not evaluated, though).

The structure factor $S(\Delta\mathbf{k})$ for scattering with wave vector transfer $\Delta\mathbf{k}$ from a lattice with average positions $\mathbf{s}_j$ and fluctuations $\mathbf{u}_j$ about those positions is

$$
\begin{aligned}
S(\Delta\mathbf{k}) &\equiv \left\langle\left|\frac{1}{\sqrt{N}}\sum_j\exp[\imath\Delta\mathbf{k}\cdot(\mathbf{s}_j+\mathbf{u}_j)]\right|^2\right\rangle\\
&=\sum_j\langle\exp[\imath\Delta\mathbf{k}\cdot(\mathbf{s}_j+\mathbf{u}_j-\mathbf{u}_0)]\rangle. \qquad (6)
\end{aligned}
$$

Thermal effects greatly reduce $S(\Delta\mathbf{k})$ at large $|\Delta\mathbf{k}|$. For diffraction by a two dimensional (2D) (planar) Bravais lattice ($\hat{z}$ denotes a unit vector perpendicular to that plane), where the parallel wave vector transfer is a monolayer reciprocal lattice vector $\mathbf{g}$, $\Delta\mathbf{k}=\Delta k_\perp\hat{z}+\mathbf{g}$, the structure factor becomes

$$
\begin{aligned}
S(\Delta\mathbf{k}) &= \sum_j\langle\exp\{\imath\Delta\mathbf{k}\cdot(\mathbf{u}_j-\mathbf{u}_0)\}\rangle\\
&=\sum_j\exp\left\{-\frac{1}{2}\langle[\Delta\mathbf{k}\cdot(\mathbf{u}_j-\mathbf{u}_0)]^2\rangle\right\}. \qquad (7)
\end{aligned}
$$

The harmonic approximation has been used in the second equality. With neglect of substrate corrugation, the perpendicular and parallel normal modes of vibration decouple,

TABLE IV. Diffraction probabilities for wave packets that satisfy scan curve conditions for excitation of the shear horizontal (SH) mode by a beam of helium atoms as function of incident energy at wave vector transfer $q=-0.125$ Å^{-1} at 2.6° from the ΓM direction. Plane of incidence is as specified in the caption of Table III. The initial wave packet is constructed as in Appendix C for the initial position and spatial width given by the specified values of NZ0 and NWI. The average, square root of the variance, and entropy S are constructed from the channel strengths (probabilities) as outlined in Appendix B. $N_>$ is the number of channels with intensity greater than that of the specular ($\mathbf{g}=0$) channel.

E_i (meV)	$I=N_{\mathrm{diff}}$						
	$I(\mathbf{g}=0)$	$\bar{I}$[a]	$\sigma(I)$	$I(\mathbf{g})_{\max}$	$S/\ln(N_{\mathrm{open}})$	N_{open}	$N_>$
2[b]	0.197	0.194	0.0697	0.273	0.952	5	2
4[b]	0.233	0.109	0.0909	0.306	0.863	9	1
5[b]	0.256	0.0765	0.0620	0.256	0.896	13	0
6[b]	0.212	0.0707	0.0494	0.212	0.918	14	0
8.2[b]	0.187	0.0466	0.0354	0.187	0.932	21	0
16.6[b]	0.0996	0.0240	0.0214	0.0996	0.905	41	0
26.5[b]	0.0407	0.0154	0.0153	0.0627	0.888	65	5
7.75[c]	0.0997	0.0516	0.0371	0.147	0.916	19	2
7.90[c]	0.201	0.0511	0.0436	0.201	0.896	19	0
8.05[c]	0.288	0.0483	0.0590	0.288	0.845	20	0
8.2[c]	0.283	0.0465	0.0561	0.283	0.858	21	0
8.35[c]	0.236	0.0458	0.0488	0.236	0.872	21	0
8.50[c]	0.238	0.0454	0.0508	0.238	0.856	22	0
8.65[c]	0.293	0.0454	0.0583	0.293	0.843	22	0

[a]The product $N_{\mathrm{open}}\bar{I}$ differs slightly from 1 because the energy width of the wave packet leads to a small diffracted intensity in nominally closed channels.
[b]NWI=100, NZ0=375.
[c]NWI=600, NZ0=1960.

$$\langle[\Delta\mathbf{k}\cdot(\mathbf{u}_j-\mathbf{u}_0)]^2\rangle=\Delta k_\perp^2\langle(u_{jz}-u_{0z})^2\rangle+\langle[\mathbf{g}\cdot(\mathbf{u}_j-\mathbf{u}_0)]^2\rangle. \tag{8}$$

The z average simplifies because the S-mode frequency $\omega_\perp$ has negligible q dependence:

$$\tfrac{1}{2}\langle(u_{jz}-u_{0z})^2\rangle\simeq\langle u_{jz}^2\rangle=\frac{\hbar}{2M\omega_\perp}\coth(\beta\hbar\omega_\perp/2). \tag{9}$$

The last term in Eq. (8) reduces to a tensor average over the normal modes:

$$\tfrac{1}{2}\langle[\mathbf{g}\cdot(\mathbf{u}_j-\mathbf{u}_0)]^2\rangle\equiv\mathbf{g}\cdot\mathbf{M}_j\cdot\mathbf{g}, \tag{10}$$

where

$$\mathbf{M}_j=(\hbar/2NM)\sum_{\mathbf{q},\nu}(1-\cos\mathbf{q}\cdot\mathbf{s}_j)\times\coth(\beta\hbar\omega_{\mathbf{q},\nu}/2)\hat{e}_{\mathbf{q},\nu}\hat{e}_{\mathbf{q},\nu}/\omega_{\mathbf{q},\nu}. \tag{11}$$

In Eq. (11), the sum goes over two polarizations ν (nominally SH and LA) with unit vectors $\hat{e}_{\mathbf{q},\nu}$ and over the N wave vectors in the first Brillouin zone. The dominant contribution to the tensor $\mathbf{M}_j$ arises from small wave numbers because of the factors $1/\omega_{\mathbf{q},\nu}$. For the assumed experimental conditions (xenon monolayer with $T\approx 50$ K), the mode populations are given by the equipartition theorem. Then, the tensor is nearly diagonal and is expressed in terms of the longitudinal and transverse speeds of sound by

$$\mathbf{M}_j\simeq\mathbf{I}(k_BT/2M)[(1/c_\ell^2)+(1/c_t^2)](1/N)\times\sum_{\mathbf{q}}(1-\cos\mathbf{q}\cdot\mathbf{s}_j)/q^2. \tag{12}$$

The sum in Eq. (12) varies logarithmically with $|\mathbf{s}_j|$ at large $|\mathbf{s}_j|$, a well-known anomaly of the 2D harmonic lattice,[17] and we evaluate the sum over neighbors in Eq. (6) for a patch containing 250 000 atoms, roughly the number of atoms on the terraces for the finest Pt(111) crystals.[30]

At low energies, E_i is comparable to the depth of the atom-monolayer potential energy [e.g., $E_i\approx 4-6$ meV and $V_0(\min)\simeq -8$ meV for He/Xe/Pt(111)]. The effect on the Debye-Waller factor is estimated using the Beeby correction,[19,20] although its reliability at such low energies E_i has not been established.[20,21] The magnitudes of the perpendicular components of the wave vector in $\Delta k_\perp=|k_{iz}|+|k_{fz}|$ are modified to reflect the inner potential:

$$|k_z|\to\sqrt{k_z^2+2mD_0/\hbar^2}, \tag{13}$$

where D_0 is the magnitude of the ground state energy of $V_0(z)$; $D_0=5.43$ meV from Table I. The final form of the Debye-Waller factor is then

$$F_{\mathrm{DW}}=\sum_j\exp[-\Delta k_\perp^2\langle u_z^2\rangle-\mathbf{g}\cdot\mathbf{M}_j\cdot\mathbf{g}]. \tag{14}$$

The Debye-Waller factor for the phonon creation strengths is estimated by using $\mathbf{g}\to\mathbf{g}-\mathbf{q}$ in Eq. (14).

TABLE V. Diffracted strengths for the cases in Table IV from a thermally excited monolayer These data are formed from the data of Table IV by multiplying by the Debye-Waller factor at 50 K, including the Beeby correction.

E_i (meV)	$I(\mathbf{g},T)=N_{\mathrm{diff}}F_{\mathrm{DW}}(50\ \mathrm{K})$						
	$I(\mathbf{g}=0)$	$\bar{I}$	$\sigma(I)$	$I(\mathbf{g})_{\max}$	$S/\ln(N_{\mathrm{open}})$	N_{open}	$N_>$
2[a]	0.108	0.087 6	0.031 3	0.123	0.953	5	1
4[a]	0.117	0.041 8	0.042 4	0.121	0.795	9	1
5[a]	0.124	0.024 5	0.031 2	0.124	0.791	13	0
6[a]	0.098 6	0.020 7	0.024 1	0.0986	0.819	14	0
8.2[a]	0.079 2	0.011 5	0.016 4	0.0792	0.800	21	0
16.6[a]	0.029 8	0.003 20	0.005 53	0.0298	0.747	41	0
26.5[a]	0.008 10	0.001 19	0.002 40	0.0129	0.695	65	2
7.75[b]	0.043 0	0.013 7	0.016 1	0.0518	0.802	19	2
7.90[b]	0.086 1	0.013 5	0.020 0	0.0861	0.756	19	0
8.05[b]	0.123	0.012 9	0.026 3	0.123	0.660	20	0
8.2[b]	0.120	0.012 3	0.024 8	0.120	0.688	21	0
8.35[b]	0.099 6	0.011 9	0.020 9	0.0996	0.723	21	0
8.50[b]	0.099 6	0.012 6	0.021 2	0.0996	0.726	22	0
8.65[b]	0.122	0.012 8	0.024 9	0.122	0.692	22	0

[a]NWI=100, NZ0=375.
[b]NWI=600, NZ0=1960.

E. Scattering rates

The solutions to Eq. (3) are used to form inelastic channel norms on the grid,

$$N_{\mathbf{q},\lambda}(\mathbf{g},t|z)=\int |S_{\mathbf{q},\lambda}(\mathbf{g},z,t)|^2 dz, \tag{15}$$

and the corresponding averages and variances of z. Similarly, the diffraction channel norm on the grid is defined by

$$N_{\mathrm{diff}}(\mathbf{g},t|z)=\int |\psi_{\mathbf{g}}(z,t)|^2 dz. \tag{16}$$

The absorbed intensities calculated with Eq. (A4) are added to these to form the net channel norms $N_{\mathbf{q},\lambda}(\mathbf{g},t)$ and $N_{\mathrm{diff}}(\mathbf{g},t)$. The final values are determined at a large enough time t_f ($t_f \gg 40$ ps for $E_i \leqslant 8$ meV) that most of the wave packet has propagated to distances more than 100 Å from the monolayer and much of the scattered intensity has been absorbed by the potential $-iU$.

The final calculated inelastic and elastic strengths incorporate additional factors and are $I_{\mathrm{inel}}(\mathbf{q},\mathbf{g},\lambda)=(k_f/k_{iz})N_{\mathbf{q},\lambda}(\mathbf{g},t_f)f_{\mathbf{q},\lambda}(T)F_{\mathrm{DW}}$ and $I_{\mathrm{el}}(\mathbf{g})=N_{\mathrm{diff}}(\mathbf{g},t_f)F_{\mathrm{DW}}$, respectively. The Debye-Waller factor F_{DW} is given in Eq. (14). I_{inel} also has a factor k_f/k_{iz}, where k_f and k_{iz} are the final wave number and perpendicular component of the initial wave vector,[31] and a factor arising from thermally excited phonons in the target monolayer:[20]

$$f_{\mathbf{q},\lambda}(T)\equiv 1+\bar{n}[\omega(\mathbf{q},\lambda)]=1/\{1-\exp[-\hbar\omega(\mathbf{q},\lambda)/k_BT]\}. \tag{17}$$

F. Interactions and scattering conditions

We use parameters and interactions for Xe/Pt(111), as given in Paper I, as representative of those for a physically adsorbed incommensurate monolayer. The normal modes of the monolayer solid are evaluated using the HFD-B2 Xe–Xe potential[32] supplemented by the McLachlan substrate-mediated dispersion energy. Some of the calculated phonon energies are listed in Table II. The pair potential between the probe atom and monolayer atoms is[33] the HFD-B2 for He–Xe and $V_0(z)$ includes the probe atom-substrate van der Waals energy $-C_3/z^3$.

The monolayer temperature is $T=50$ K and the scan curve angle between the incident wave vector and the $\mathbf{g}=0$ outgoing beam in Ψ_1 is $\Theta_{\mathrm{SD}}=95.8°$. See also Fig. 1. The misalignment of the scattering plane relative to the ΓM azimuth of the monolayer is $\alpha=2.6°$, the Novaco-McTague orientational alignment angle at $L_{\mathrm{nn}}=4.33$ Å determined in the Xe/Pt(111) experiments.[6] This value is not crucial because a misalignment $\alpha=0.5°$ also gives strong symmetry-breaking SH-mode excitation[9] Mostly, the phonon wave vectors are directed antiparallel to $\mathbf{k}_{i\|}$ because of the experimental experience[6] that this led to better resolved SH-mode excitation.

III. SCATTERING RESULTS

The wave packet scattering is evaluated for a basic set of 24 cases formed from two polarizations (SH and LA), two wave numbers (–0.125 and –0.25 Å^{-1}), and six incident energies E_i in the range 4–26.5 meV. These are augmented by two series of cases for the SH mode at $E_i \simeq 8$ meV: one is a scan with $\Delta E_i=0.15$ meV at –0.125 Å^{-1} and the other is a scan over $\mathbf{q}$ at $E_i=8.2$ meV. There are a few cases for E_i near the threshold for creating the phonons. From Table II, the SH mode has energy up to 2.2 meV and the LA mode up to 4 meV for the q's in our calculations.

We begin with some general remarks on the relative strengths in the specular and nonspecular channels. The full discussion for relatively narrow wave packets is given for diffraction in Sec. III A, for inelastic scattering in Sec. III B, and for broader packets with higher energy resolution in Sec. III C.

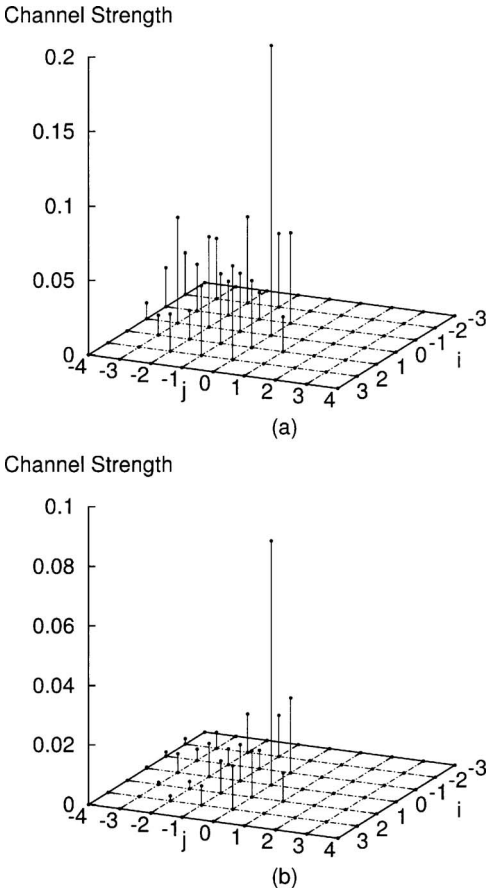

FIG. 3. The distribution of the elastic strengths over open channels for E_i =8.2 meV and Θ_i=44.20°. The channel labels (i,j) specify the reciprocal lattice vector $\mathbf{g}=i\mathbf{g}_1+j\mathbf{g}_2$ of length $g=g_0\sqrt{i^2+j^2-ij}$. The specular channel has $i=j=0$. The scattering geometry is for the LA phonon at $\mathbf{q}=-0.125$ Å^{-1}, as specified in the caption of Fig. 2. (a) Channel norms N_{diff} determined directly in the simulations. (b) Channel strengths $I_{\mathrm{el}}(\mathbf{q})$ with the Debye-Waller factor at 50 K included.

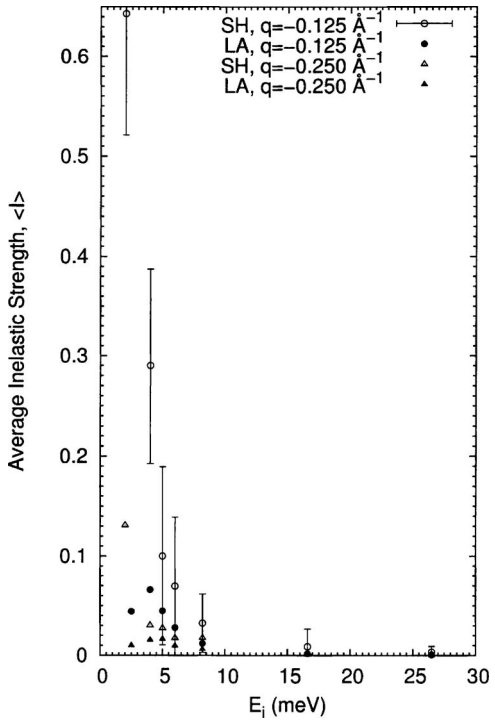

FIG. 4. The average inelastic strength $\langle I\rangle=\bar{I}_{\mathrm{inel}}(\mathbf{q},\lambda)$ as a function of initial energy E_i for creating SH and LA phonons in the scattering geometry specified in the captions of Fig. 2 and Table III. The strength includes thermal factors at 50 K and flux factors as described in Sec. II E. The error bars denote the standard deviation of the average for the SH $q=-0.125$ Å^{-1} series; those for the other three series are similar but omitted in the plot for clarity. Energies E_i are in meV and wave numbers q in Å^{-1}. Open symbols denote SH polarization and filled symbols LA polarization.

The Xe monolayer is a very corrugated target[33,34] and the scattering is the result of strong coupling of the ^{4}He to the monolayer. Thus, it was expected that there would be much diffracted strength in nonspecular $\mathbf{g}\neq 0$ channels. This is fulfilled in all the cases we studied, although the strength in the specular channel $I_{\mathrm{el}}(\mathbf{g}=0)$ generally is higher than the average $\bar{I}_{\mathrm{el}}$. For $E_i<8$ meV, the specular channel in Ψ_0 is almost always the strongest one. Near 8 meV, the specular intensity has significant nonmonotonic variations over increments $\Delta E_i=0.15$ meV.

It was also expected that there would be significant probability for exciting the SH mode in $\mathbf{g}\neq 0$ channels, as that is how the polarization selection rules are overcome in the weak coupling theory of inelastic neutron scattering.[2] However, HAS does excite the SH mode in the first Brillouin zone near symmetry azimuths, which was not anticipated before the experiments were performed.[6] A remarkable result of the strong coupling calculations is that the strength $N_{\mathbf{q},\mathrm{SH}}(\mathbf{g}=0)$ in the specular channel frequently is largest or nearly the largest for $E_i<10$ meV. Further, the $\mathbf{g}=0$ inelastic strengths and the total (over all open channels) inelastic strengths $I_{\mathrm{inel}}(\mathrm{tot})$ generally are larger for the SH excitations than for the LA excitations at given E_i and $\mathbf{q}$. This too is an effect of the strong coupling and is markedly different from that expected for weak coupling, as in neutron scattering.[2]

A. Diffraction

The diffraction calculation (Ψ_0) is linked to the inelastic scattering calculation because the angle of incidence Θ_i is set by the scan curve condition. Thus, for many of the incident energies E_i, we have several calculations of the distribution of diffracted strengths. The angles Θ_i are presented in Table III.

Except at energies $E_i<5$ meV, overall trends for the diffraction are insensitive to the changes in Θ_i that arise in satisfying the scan curve constraints for excitations with different $\mathbf{q}$ and polarization. This is shown for $\bar{I}(E_i)$ [the average of $I_{\mathrm{el}}(\mathbf{g})$ over open channels as a function of incident energy] in Fig. 2. The error bars in Fig. 2 and subsequent figures represent the standard deviation in an average over channels; the strength in a given channel is calculated with a precision better than 1%. Although the strength in a given channel is the result of a complicated pattern of couplings between all channels in Ψ_0, $\bar{I}(E_i)$ clearly decreases with increasing E_i. For the N_{diff}, there is a conservation law and $\bar{I}=1/N_{\mathrm{open}}$, where N_{open} is the (energy-dependent) number of open diffraction channels. As E_i increases, N_{open} increases linearly with E_i, as shown in Table IV, and the $\bar{I}$ in Table IV varies as $1/E_i$. The effect of the Debye-Waller factor is to

TABLE VI. Summary of the specular inelastic strengths $I_{\mathrm{inel}}(\mathbf{q},\mathbf{g}=0,\lambda)$ at $T=50$ K as a function of incident energy E_i (in meV) for λ=SH and LA. Wave numbers q are given in Å^{-1}; the plane of incidence and the orientation of the wave vectors are as specified in the caption of Table III. Except as noted, the initial wave packet has NWI=100 and NZ0=375.

q	−0.125	−0.25	−0.5	−0.125	−0.25	−0.5
E_i		SH			LA	
2.0	0.615	0.179				
2.5				0.0417	0.013	
4.0	0.418	0.0184[a]		0.0482	0.0082	
5.0	0.323	0.0182[a]	0.0153	0.0913	0.0097	0.0053
6.0	0.263	0.101[a]		0.0665	0.0154	
8.2[b]	0.0654[a]	0.0209[a]	0.0160	0.0220	0.0183	0.0092
16.6[c]	0.0243	0.0013[a]		0.0044	0.0020	
26.5	0.0050	0.0018[a]		0.0020	0.0007	

[a]NWI=600, NZ0=1960.
[b]The SH entries for $q=0.125$, 0.25, and 0.5 are 0.0575, 0.0269, and 0.0109, respectively.
[c]The S-mode values for $q=-0.25$, −0.125, 0.125, 0.25, and 0.5 are 0.026, 0.031, 0.035, 0.043, and 0.043, respectively.

reduce markedly the contributions from many of the open channels, and the net variation of $\bar{I}$ in Table V and Fig. 2 is close to $1/E_i^2$.

Tables IV and V give a rather full characterization of the distribution of diffracted strength over open channels for a series of incident energies with Θ_i set by the scan curve condition for the SH mode at $\mathbf{q}=-0.125$ Å^{-1}, the first being based on N_{diff} [Eq. (16)] and the second on $I_{\mathrm{el}}(\mathbf{g})$ [including the Debye-Waller factor]. The first column is the incident energy and the second is the strength of the $\mathbf{g}=0$ peak. The remaining columns give a sense of the statistical nature of the distributions as formulated in Appendix B, presenting the average over open channels, its standard deviation (defined to be the square root of the variance for these non-Gaussian distributions), the maximum channel strength, the fractional entropy, and the numbers of open channels and of those with strengths greater than the $\mathbf{g}=0$ strength. Comparing the tables shows the marked changes in the distributions that arise by including the Debye-Waller factor for thermal attenuation. Figure 3 graphically shows these changes for another case with $E_i=8.2$ meV.

The relatively large ratios $\sigma/\bar{I}$ and $S/\ln(N_{\mathrm{open}})$ in Tables IV and V demonstrate the statistical nature of the distributions arising from the "deterministic" wave packet propagation in a strong coupling regime. The Debye-Waller factor decreases the strength for channels with large $|\mathbf{g}|$, Table V, so that the distribution is concentrated in fewer channels and the fractional entropy tends to be smaller at the larger values of E_i. A significant part of the statistical character arises from the energy width of the wave packet, which was demonstrated by comparing the fractional entropies for packets with NWI=100 and 600 (e.g., compare the two sets of entries for $E_i=8.2$ meV in these tables). The NWI parameter regulates the width of the initial wave packet as defined in Appendix C. The fractional entropies usually were smaller for larger values of NWI, consistent with more order in a more monochromatic scattering event.

B. Inelastic strengths

Figure 4 and Tables VI and VII give an overview of the energy dependence of the strengths of SH and LA excitations created by inelastic atomic scattering. It is very clear that the SH branch is much stronger than the LA branch at energies below 10 meV and that this feature is not restricted to special choices of E_i. Tables VIII and IX are fuller characterizations

TABLE VII. Summary of the total inelastic strengths $I_{\mathrm{tot}}(\mathbf{q},\lambda)$ at 50 K as a function of incident energy E_i (in meV) for λ=SH and LA for the same cases as in Table VI. Wave numbers q are given in Å^{-1}. Initial wave packets are as specified in Table VI.

q	−0.125	−0.25	−0.5	−0.125	−0.25	−0.5
E_i		SH			LA	
2.0	2.58	0.261				
2.5				0.18	0.021	
4.0	2.03	0.212		0.46	0.11	
5.0	1.10	0.248	0.07	0.40	0.12	0.024
6.0	0.98	0.211		0.34	0.09	
8.2[a]	0.62	0.303	0.095	0.21	0.09	0.038
16.6[b]	0.35	0.114		0.08	0.03	
26.5	0.21	0.080		0.04	0.01	

[a]The SH entries for $q=0.125$, 0.25, and 0.5 are 0.46, 0.14, and 0.068, respectively.
[b]The S-mode values at 16.6 meV for $q=-0.25$, −0.125, 0.125, 0.25, and 0.5 are 0.136, 0.167, 0.182, 0.180, and 0.177, respectively.

TABLE VIII. The excitation of the shear horizontal (SH) mode by a beam of helium atoms as function of incident energy at wave vector transfer $q=-0.125$ Å^{-1} at 2.6° from the ΓM direction. Plane of incidence is as specified in the caption of Table III. Inelastic scattering with the initial wave packet described in the caption of Table IV. The strengths $I(\mathbf{g})$ are the channel norms $N_{\mathbf{q},\lambda}(\mathbf{g})$ defined in Sec. II E.

E_i (meV)	$I(\mathbf{g})=N_{\mathbf{q},\mathrm{SH}}(\mathbf{g})$						
	$I(\mathbf{g}=0)$	$\bar{I}$	$\sigma(I)$	$I(\mathbf{g})_{\max}$	$S/\ln(N_{\mathrm{open}})$	N_{open}	$N_>$
2[a]	0.140	0.166	0.0379	0.220	0.981	4	2
4[a]	0.0868	0.0799	0.0165	0.105	0.989	7	3
5[a]	0.0675	0.0309	0.0166	0.0675	0.949	11	0
6[a]	0.0561	0.0239	0.0151	0.0561	0.929	14	0
8.2[a]	0.0168	0.0175	0.0986	0.0426	0.946	19	9
16.6[a]	0.00744	0.00705	0.00633	0.0266	0.913	40	7
26.5[a]	0.00226	0.00518	0.00631	0.0259	0.856	63	35
7.75[b]	0.0635	0.0289	0.0252	0.0945	0.870	17	1
7.90[b]	0.0313	0.0226	0.0189	0.0655	0.884	18	5
8.05[b]	0.0242	0.0187	0.0131	0.0551	0.914	18	5
8.2[b]	0.0148	0.0153	0.00962	0.0355	0.925	19	9
8.35[b]	0.00427	0.0123	0.00766	0.0259	0.928	19	15
8.50[b]	0.0080	0.0103	0.00979	0.0339	0.853	19	18
8.65[b]	0.00488	0.00968	0.00907	0.0329	0.871	19	12

[a]NWI=100, NZ0=375.
[b]NWI=600, NZ0=1960.

of the inelastic scattering for the SH mode with $q=-0.125$ Å^{-1} (generally the strongest of the excitation processes). The role of the Debye-Waller factor in modifying the distribution of strengths over channels is illustrated in Fig. 5 for the LA mode at $q=-0.125$ Å^{-1} and 8.2 meV; in this rather extreme case, including the Debye-Waller factor decreases the value of $N_>$ from 10 to 1.

To assure convergence of the calculations for the inelastic scattering, the wave packet must be propagated for a longer time than would be decided from an analysis of Ψ_0 alone. For a given scattering event, the norm of Ψ_1 grows rapidly with time after the turning point (i.e., the time t_t when the average $\langle z\rangle_{\Psi_0}$ is a minimum) as the elastic wave (Ψ_0) recedes from the monolayer. The division of strength among the open channels evolves for rather long times, especially at smaller E_i where there is more transient strength in closed channels. At the higher energies, $E_i=16.6$ and 26.5 meV, there are many open channels ($\approx$40–60) for both the elastic and inelastic scattering, and the strengths in individual channels become smaller. Time scales are shorter, in

TABLE IX. Strengths of excitation of the shear horizontal (SH) mode by a beam of helium atoms from a thermally excited monolayer as function of incident energy at wave vector transfer $q=-0.125$ Å^{-1} for the same cases as in Table VIII. These strengths are the final $I_{\mathrm{inel}}(\mathbf{q},\mathbf{g},\mathrm{SH})$ of Sec. II E obtained from the data of Table VIII by correcting for flux factors and thermal excitation effects at 50 K.

E_i (meV)	$I(\mathbf{g})=I_{\mathrm{inel}}(\mathbf{q},\mathbf{g},\mathrm{SH})$						
	$I(\mathbf{g}=0)$	$\bar{I}$	$\sigma(I)$	$I(\mathbf{g})_{\max}$	$S/\ln(N_{\mathrm{open}})$	N_{open}	$N_>$
2[a]	0.615	0.644	0.122	0.809	0.987	4	2
4[a]	0.418	0.290	0.097 2	0.418	0.970	7	0
5[a]	0.323	0.100	0.089 6	0.323	0.865	11	0
6[a]	0.263	0.069 7	0.069 4	0.263	0.851	14	0
8.2[a]	0.074 1	0.040 9	0.040 2	0.154	0.850	19	2
16.6[a]	0.024 3	0.008 80	0.011 8	0.0491	0.795	40	4
26.6[a]	0.005 02	0.003 38	0.005 82	0.0225	0.733	63	13
7.75[b]	0.284	0.081 0	0.099 6	0.348	0.770	17	1
7.90[b]	0.139	0.062 0	0.072 4	0.239	0.789	18	2
8.05[b]	0.107	0.046 6	0.050 9	0.198	0.820	18	2
8.2[b]	0.065 4	0.032 5	0.029 3	0.112	0.860	19	2
8.35[b]	0.018 8	0.023 3	0.018 9	0.0566	0.880	19	8
8.50[b]	0.003 5	0.021 9	0.027 4	0.0967	0.773	19	13
8.65[b]	0.021 3	0.021 5	0.030 3	0.105	0.757	19	3

[a]NWI=100, NZ0=375.
[b]NWI=600, NZ0=1960.

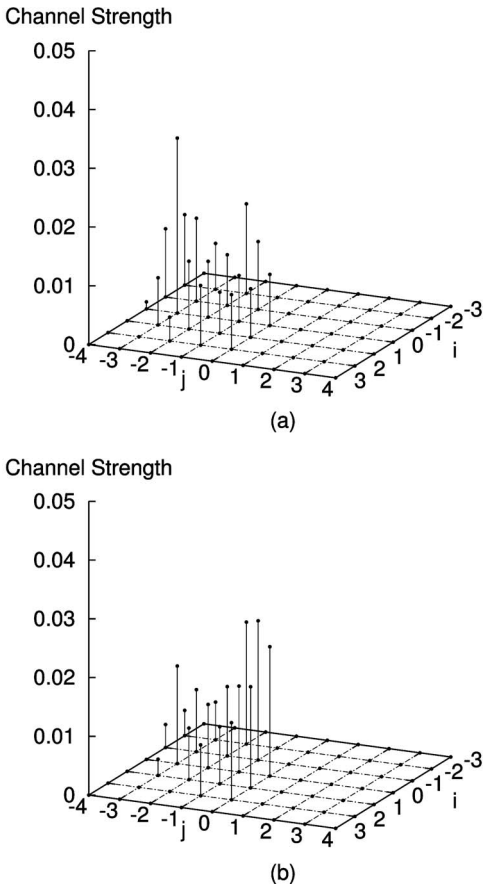

FIG. 5. The distribution of the inelastic strength over open channels for creating a LA phonon with wave number $q=-0.125$ Å^{-1} at $E_i=8.2$ meV. The corresponding distribution of elastic strength is shown in Fig. 3, which also has the definition of the channel labels (i,j). The geometry is the same as in Fig. 3. (a) Channel norms $N_{\mathbf{q},\mathrm{LA}}(\mathbf{g})$. Ten channels have strengths greater than the specular (0,0) one. (b) Channel strengths $I_{\mathrm{inel}}(\mathbf{q},\mathbf{g},\mathrm{LA})$ including Debye-Waller factor, flux factors, and thermally excited phonons at 50 K. The $(-1,-1)$ channel is the strongest, followed by the (0,0) channel, and then the $(-2,-2)$ channel.

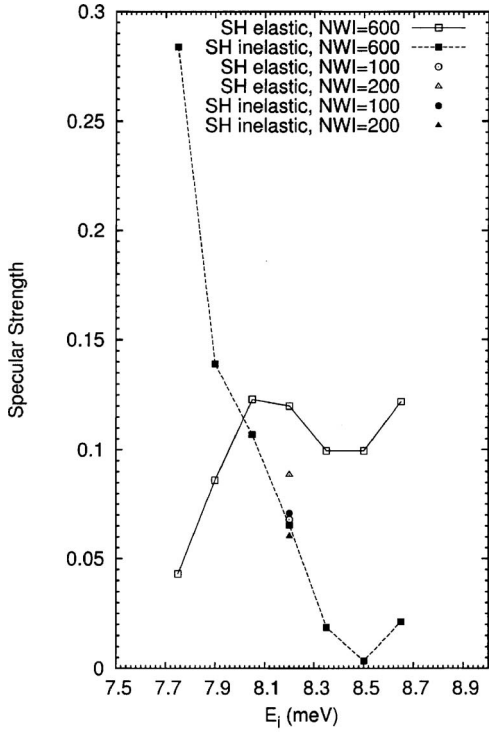

FIG. 6. High energy resolution results at 50 K for the strengths I in the specular for the strengths in the specular ($\mathbf{g}=0$) elastic and inelastic channels for scattering at the SH $q=-0.125$ Å^{-1} scan curve conditions. A broad spatial packet of width NWI=600 is used, corresponding to a standard deviation in the initial z component of the wave vector $\sigma_{k_{iz}}=1.96\times10^{-2}$ Å^{-1} and in the initial energy $\sigma_E=5.7\times10^{-2}$ meV. The plane of incidence and orientation of the wave vector are as specified in the caption of Fig. 2. The dashed and solid lines are guides for the eye, linking points calculated at an energy spacing $\Delta E_i=0.15$ meV. At $E_i=8.2$ meV, two more sets of points for NWI=100 ($\sigma_{k_{iz}}=1.18\times10^{-1}$ Å^{-1} and $\sigma_E=3.4\times10^{-1}$ meV) and NWI=200 ($\sigma_{k_{iz}}=5.88\times10^{-2}$ Å^{-1} and $\sigma_E=1.7\times10^{-1}$ meV) are shown to illustrate the dependence on NWI. Open symbols denote the elastic scattering and filled symbols the inelastic scattering.

part because the speed of the probe atom is greater for given energy loss $\hbar\omega(\mathbf{q},\lambda)$. There is a rather fast development of the inelastic beams, as measured by the difference between the time at which the norm of Ψ_1 reaches 75% of its final value and the turning point time t_t for Ψ_0.

We can identify some general trends in the results for $I_{\mathrm{inel}}(\mathbf{q},\mathbf{g},\lambda)$, $\lambda=$SH and LA. Except for the lowest values of E_i used in these calculations (2 and 2.5 meV), the total inelastic strength $I_{\mathrm{tot}}(\mathbf{q},\lambda)$ decreases as E_i increases. The number of open inelastic channels increases from 7 at 4 meV to about 60 at 26.5 meV. The strength in a given open channel tends to be larger for smaller E_i, i.e., the excitation of the dispersive long wavelength phonons is stronger at low, but above-threshold, incident energy. $I_{\mathrm{inel}}(\mathbf{g}=0)$ is greater than $\bar{I}_{\mathrm{inel}}$ in most of the cases for both the SH and LA branches. Also, even with the Debye-Waller attenuation of the nonspecular channels, the distribution of inelastic strength over channels remains quite statistical with ratios $\sigma/\bar{I}$ of order 1 in most cases. For given $\mathbf{q}$ and polarization λ, the fractional entropy $S/\ln(N_{\mathrm{open}})$ tends to decrease as E_i increases from 4 to 25 meV.

However, there are special conditions where the specular channel strength is much larger than anticipated from statistical considerations. For example, the SH phonon of $q=-0.25$ Å^{-1} at $E_i=6$ meV has $I_{\mathrm{inel}}(\mathbf{g}=0)/\bar{I}_{\mathrm{inel}}\simeq 6$, while the ratio is 0.7 and 1.2 at $E_i=5$ and 8.2 meV, respectively. The occasional very strong inelastic peaks found in the experiments[6,10] are also indications of such sensitivity. There are optimal energies in the calculations, depending on the wave number and the polarization, for phonon excitation both in an individual channel and for the total inelastic strength, Tables VI and VII. The total inelastic strength for these SH phonons has a maximum at E_i in the range 2–5 meV.

The inelastic strength $I_{\mathrm{inel}}(\mathbf{g}=0)$ for $q=-0.125$ Å^{-1} is higher than for $q=-0.25$ Å^{-1} for the SH and the LA series. In several cases, though, the margin in the comparison comes from the factor $1+\bar{n}$, Eq. (17), rather than the intrinsic strengths $N_{\mathbf{q}\lambda}$.

The calculations give inelastic strengths for the nonspecular $\mathbf{g}\neq 0$ channels which were not measured in most of the HAS experiments. As already noted, one surprise for the SH branch is that the specular channel is the strongest one at 4–6 meV for $q=-0.125$ Å^{-1}. For $q=-0.25$ Å^{-1}, the strongest SH scattering was in nonspecular channels for five of

the seven values of E_i that were studied. Although the excitation of the LA branch in the first Brillouin zone does not depend crucially on the small misalignment of the scattering plane (i.e., no selection rule to be broken), the occurrence of strong nonspecular inelastic peaks for the LA cases has much similarity to the SH cases.

The excitation of the SH mode has been calculated as a function of q from -0.5 Å^{-1} to the Brillouin zone boundary value, at a 2.6° misalignment with the ΓM direction and constant $E_i=8.2$ meV. Some of the results are given in Table VI. The trends for the channel norms $N_{\mathbf{q},\mathrm{SH}}$ and the final calculated strength $I_{\mathrm{inel}}(\mathbf{q},\mathbf{g},\mathrm{SH})$ are markedly different because the thermal factor $1+\bar{n}$, Eq. (17), strongly enhances the small $|\mathbf{q}|$ strength, both for the specular channel and the total $I_{\mathrm{tot}}(\mathbf{q},\mathrm{SH})$. The asymmetry between the $\pm\mathbf{q}$ cases arises from the differences in initial conditions ($\mathbf{k}_i$) to satisfy the scan curve constraints. The total inelastic strengths are 30% to 100% larger for the negative q cases.[31]

The decreases of $I_{\mathrm{inel}}(\mathbf{q},\mathbf{g}=0,\mathrm{SH})$ with increasing $|\mathbf{q}|$ occurs also at $E_i=5$ meV and the trend is also present in the results for the LA mode. A decrease with increasing $|\mathbf{q}|$ near the Brillouin zone center that results from the intrinsic scattering (form factors) has been known for some time[20] but these calculations show the very important role of the thermal factor $1+\bar{n}$ for dispersive branches.

Our calculations for the S mode are much less extensive and consist mainly of a scan of the wave vector dependence of the excitation at $E_i=16.6$ meV, the energy used in a recent measurement.[6] In contrast to the other branches, the strongest inelastic channel is the specular one for $q=-0.25$ to 0.5 Å^{-1} at 2.6° to the ΓM axis. The dependence of $I_{\mathrm{inel}}(\mathbf{q},\mathbf{g}=0,\mathrm{S})$ on $|\mathbf{q}|$ is much smaller for the S mode with its nearly dispersionless frequency $\omega_\perp=3.5$ meV; some values at $E_i=16.6$ meV are included in Tables VI and VII.

C. Higher energy resolution

There are suggestions of significant energy dependence for channel strengths in the data presented thus far. To explore this more thoroughly, we made a series of calculations with packets that have narrower energy spreads, using a spatial width NWI=600. An overview of the results is given in Fig. 6, which shows the strengths $I_{\mathrm{el}}(\mathbf{g}=0)$ and $I_{\mathrm{inel}}(q=-0.125,\mathbf{g}=0,\mathrm{SH})$ on a grid with $\Delta E_i=0.15$ meV. There clearly is a strong energy dependence to the inelastic scattering and also a marked variation of the specular elastic strength. The channel strengths vary strongly with incident energy E_i in a nonmonotone way. Calculations, and experiments, with broader energy distribution in the incident beam result in scattering strengths that are averaged over fine details in the spectrum. The fuller statistical analyses are presented in Tables IV, V, VIII, and IX.

The sensitivity to the spatial width is present in other examples too. For instance, at $E_i=6$ meV, $I_{\mathrm{inel}}(q=-0.25$ Å$^{-1},\mathbf{g}=0,\mathrm{SH})$ is 0.018 for NWI=600 and is 0.026 for NWI=100.

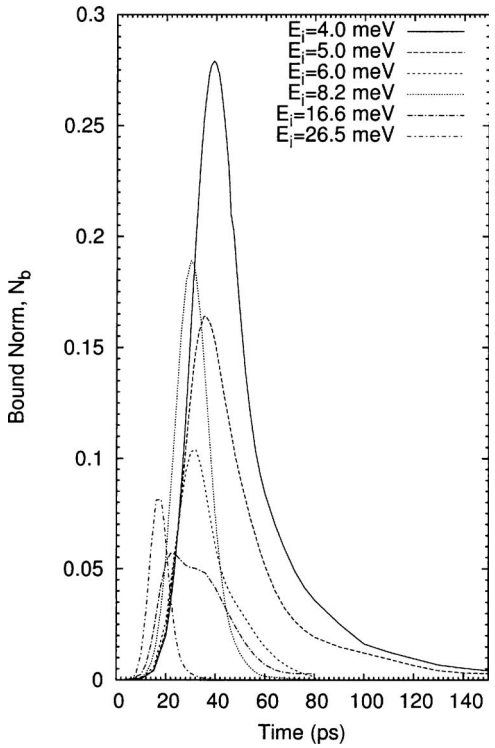

FIG. 7. The bound norm N_b as a function of time (in ps) at six incident energies E_i for the elastic wave Ψ_0 that arises in simulating the inelastic excitation of SH phonons of $q=-0.25$ Å^{-1}. The plane of incidence and wave vector are as specified in the caption of Fig. 2. The initial wave packets have NWI=600 and are centered at $z_0=119$ Å. For reference, the times (in ps) at the turning point are $t_t=35.4$, 32.2, 29.4, 26.3, 18.6, and 14.9 for $E_i=4$, 5, 6, 8.2, 16.6, and 26.5 meV.

IV. ANALYSIS OF TRANSIENT TRAPPING

A. Transient trapping in elastic scattering

Many closed channels are populated during the elastic scattering, but at sufficiently large times, those norms eventually decay to zero via couplings to the open channels and all of the norm is in outgoing channels because there is no mechanism in Eq. (2) for the formation of permanently trapped probe atoms. We calculate the transiently bound ("trapped") norm $N_b(t)$ by projecting the channel amplitudes $\psi_{\mathbf{g}}(z,t)$ onto the bound eigenstates of V_0 for all channels, whether nominally closed or open. The evolution of the total bound intensity $N_b(t)$ is shown for several energies E_i in Fig. 7; in this series, the initial wave packet is centered at $z_0=119$ Å and has a turning point near 20 Å at a time $t_t=35-15$ ps for $E_i=4-26.5$ meV. For other polarization and wave vector combinations, the Θ_i are different and there are changes in the detailed time evolution. For instance, in some series the maximum of N_b decreases monotonically as E_i increases although that is not the behavior in Fig. 7. Because the construction of N_b does not allow for the 2D band structure of the selective adsorption states, there is a small error which becomes significant at large times and limits our analysis to time ranges where N_b is greater than 0.001.

The norm N_b initially increases to a maximum at a few picoseconds after the wave packet turns. Beyond the maximum, we fit the time dependence of N_b to one or two exponential decay terms:

$$N_b(t) = A_1 \exp(-t/\tau_1) + A_2 \exp(-t/\tau_2). \quad (18)$$

Results for the decay times τ are given in Table III for initial conditions on Ψ_0 set by the scan curve constraints for the SH and LA modes at two wave vectors $\mathbf{q}$. (The amplitudes A_j are not given there.) In several cases, statistically significant fits were only obtained using one term and there is no entry for τ_2. In most of the low energy cases ($E_i \leqslant 5$ meV), there was a long decay time τ_2 and much of the data range for those cases was dominated by that term. One of the 16.6 meV cases (SH, $q=-0.25$ Å^{-1}) has an unusual evolution of N_b, which persists at values near its maximum for more than 20 ps as shown in Fig. 7. That case has large transient population in two channels closed by $\Delta < 0.2$ meV, but does not seem to be correlated to strong inelastic scattering.

There are competing processes that create a closed channel with a wave function $\psi_{\mathbf{g}}$ localized near the monolayer that has a long-lived norm in the scattering event. Channels with small energy deficit $|\Delta|$ are all coupled to at least one open channel by a term $V(g_0,z)$, which nominally is strong. However, the $\psi_{\mathbf{g}}$ of such channels mostly overlaps shallow bound states of V_0 with probability concentrated far enough from the surface that $V(g_0,z)$ is small. That slows the desorption process. For the channels with larger $|\Delta|$, the desorption may also be slow because the coupling to open channels either goes by a larger wave vector transfer or by first mixing with channels of small $|\Delta|$. An analysis using the "density" of closed states in narrow ranges of Δ, which can be done without the scattering solution, helps to identify initial conditions likely to lead to strong transient trapping. Concentrations (or degeneracies) in the number of channels in energy ranges overlapping the bound states of V_0 correlate rather well with the strongest trapping cases.

In summary, the decay times τ in Table III demonstrate that there are many cases with long times for completion of the elastic scattering.[13] It takes some tens of picoseconds after the turning point of the scattering to reach a time when more than 95% of the norm of Ψ_0 is in outgoing channels. This effect is particularly marked at $E_i < 8$ meV.

B. Permanently trapped probe atoms

Probe atoms with very long trapping times may be produced in a low energy inelastic scattering event if sufficient energy is transferred to the target monolayer. In the one-phonon loss approximation used here, there is no mechanism for the probe atom to recover enough energy to escape again. We have demonstrated the trapping for the LA mode at $q=-0.25$ Å^{-1} and $E_i=2.5$ meV with two simulations which differ slightly in the angle of incidence Θ_i. In a case with $\Theta_i=13.9°$ there is no open final channel in Ψ_1, while for $\Theta_i=13.7°$ there is one open channel in Ψ_1. For both cases there are six open channels in Ψ_0.

The decay of the transiently bound norm $N_b(t)$ for Ψ_0 is very slow and the simulations were continued beyond 280 ps to reach times where $N_b < 0.002$. The results of a fit to two exponentials are given in Table III. The decay times are very different, one at about 10 ps and a much longer one of about 100 ps. The decay apparently is a little slower in the case with one open Ψ_1 channel, probably because this has more closed Ψ_0 channels of very small $|\Delta|$.

The distribution of inelastic strength over channels did not tend to a limit in either case, even for times beyond 400 ps. We have generally used the large time behavior of the specular channel norm $N_{\mathbf{q},\lambda}(\mathbf{g}=0,t)$, Eq. (15), as the diagnostic for completion of the scattering event. However, for these cases at $E_i=2.5$ meV, this channel norm continued to oscillate and did not converge to a limit at $t \approx 400$ ps. Other cases could be propagated to such large times that most of the total inelastic strength became absorbed by the potential $-iU$. For these two cases, only a small part of the inelastic strength was absorbed and most of the inelastic strength remained on the spatial grid. Thus, the probe atom has been trapped by the monolayer and the oscillation of the inelastic strength in the specular channel arises from an exchange of strength between a few channels with wave functions $S_{\mathbf{q},\mathrm{LA}}(\mathbf{g},z,t)$ that are localized near the surface.

V. CONCLUSIONS

Our results confirm that the excitation of the SH branch for scattering planes at small misalignment to symmetry azimuths of the monolayer lattice is a robust phenomenon and show that it is enhanced at low incident energy. Remarkably, both the specular inelastic strength and the total inelastic strength increase steadily as the energy decreases below $E_i \approx 6$ meV. The SH branch can be readily excited in HAS experiments at low incident energies without invoking effects of defects or of second layer gas above the monolayer solid. The excitation of the LA phonons is also enhanced by using low incident energies, below 10 meV or so.

At given E_i, the final calculated inelastic strengths $I_{\mathrm{inel}}(\mathbf{q},g=0,\lambda)$ decrease as $|\mathbf{q}|$ increases for both the SH and LA modes. This is shown explicitly at $E_i=5$ and 8.2 meV in Table VI. In many of the cases, the enhancement by thermally excited phonons, Eq. (17), is an important contribution to making the inelastic strength for SH greater than for LA excitations at the same $\mathbf{q}$.

Thus, thermal effects play an important role in determining the strength distributions for both the elastic and inelastic atomic scattering. These include an enhancement of the low-q strengths by thermally excited phonons and the Debye-Waller-factor attenuation of scatterings with large reciprocal lattice vector transfers. This arises because in the HAS experiments thus far, a common working temperature has been 40–50 K, which leads to an appreciable thermal excitation of the target.

The sensitivity of the calculations to Θ_i and the specifics of the scan curve construction limit the transferability of the detailed results to other experimental configurations. For instance, the Θ_i for the SH $q=-0.125$ Å^{-1} mode at 8.2 meV changes from 45.2° to 42.5° when Θ_{SD} changes from 95.8° to 90°. The qualitative features we have identified do survive. To derive full information from low energy inelastic atomic scattering experiments, the work will have to be accompanied by scattering calculations such as those presented here.

ACKNOWLEDGMENTS

We thank Dr. S. P. Johnson and Dr. C. S. Lerotheou who used ParaWise to carry out the parallelization of our code and Dr. Bernd Dammann, Informatics and Mathematical Modeling, Technical University of Denmark, for helping us to run the code on the Sun Machines at DTU. Further information about ParaWise is available at www.parallelsp.com.

APPENDIX A: TIME PROPAGATION WITH AN ABSORBING POTENTIAL

The general form of the time-dependent Schrödinger equation for the wave function of the scattered (^{4}He) atom is

$$i\hbar\partial\Psi/\partial t = (K + V - iU)\Psi, \tag{A1}$$

where K denotes the kinetic energy operator, V is the atom-monolayer potential energy, and $-iU$ is an absorbing potential that is introduced to eliminate reflections of the outgoing atom from the large-z boundary. For $U=0$, we found[9] that the time development was given very stably by a simple second-order stepping procedure, using a fast Fourier transform to evaluate the effect of K:

$$\Psi(t + dt) = \Psi(t - dt) - 2dt(\imath/\hbar)(K + V)\Psi(t). \tag{A2}$$

With the absorbing potential ($U>0$ leads to a loss of probability), we adopt

$$\Psi(t + dt) = \left[1 - \frac{U}{\hbar}2dt\right]\Psi(t - dt) - 2dt(\imath/\hbar)(K + V)\Psi(t). \tag{A3}$$

This propagation is stable according to the formal analysis of Koonin[27] and also in our experience with the numerical implementation.

The totals $\int|\Psi_j|^2 d\mathbf{r}(j=0,1)$ decrease at large times as components of the outgoing wave packet are absorbed. As a check on the stability of the calculation, we monitored the current in each channel, $J_z(\mathbf{g}) = (\hbar/2mi)[\chi_\mathbf{g}^* \partial\chi_\mathbf{g}/\partial z - \chi_\mathbf{g}\partial\chi_\mathbf{g}^*/\partial z]$, just before z_U [Eq. (5)], and calculated the total absorbed current as

$$I_{\mathrm{abs}}(\mathbf{g},t) = \int_0^t J_z(\mathbf{g},t')dt', \tag{A4}$$

where χ is $\psi_\mathbf{g}$ or $S_{\mathbf{q},\lambda}(\mathbf{g})$ [Eq. (2) or (3)] for the diffractive and inelastic scattering, respectively. The total of the Ψ_0 norm on the spatial (z) grid and its accumulated current into the absorber remained constant over the total propagation time to a few parts in 10^4.

APPENDIX B: ENTROPY ANALYSIS OF STRENGTH DISTRIBUTIONS

The scattering calculations give so much information that we have used some statistical measures to get an overview of the data. These are the average, square root of the variance, and information theory entropy for the channel strengths of either the elastic or the inelastic scattering.

Let the strengths in the η open channels be denoted by s_j. The average (mean) and mean-square strengths are then defined by

$$\bar{s} \equiv \sum_{j=1}^{\eta} s_j/\eta, \quad \overline{s^2} \equiv \sum_{j=1}^{\eta} s_j^2/\eta, \tag{B1}$$

and the standard deviation (square root of variance) is $\sigma \equiv \sqrt{\overline{s^2} - \bar{s}^2}$.

For the entropy S, define the normalized weights constructed from the s_j,

$$p_i \equiv s_i/\sum_{j=1}^{\eta} s_j = s_i/\eta\bar{s}, \tag{B2}$$

and then form[23]

$$S = -\sum_{j=1}^{\eta} p_j \ln p_j. \tag{B3}$$

Convexity relations[22] give general upper and lower bounds on the entropy. For a function f with positive second derivative, the convexity bound on the average is $\langle f(x)\rangle \geqslant f(\langle x\rangle)$ and the sense reverses for negative second derivative. A lower bound is obtained using $x=p_j$ and $f(x)=\ln x$ and an upper bound with $x=1/p_j$ and $f(x)=-\ln x$:

$$\ln\,\eta - \ln(\overline{s^2}/\bar{s}^2) \leqslant S \leqslant \ln\,\eta. \tag{B4}$$

The fractional entropy $S/\ln\,\eta$ is used to follow trends for these non-Gaussian distributions; it is 1 for a uniform (random) distribution.

APPENDIX C: IMPLEMENTATION OF THE WAVE PACKET CALCULATION

The initial wave packet has the following form:

$$\Psi_i(\mathbf{r},z) = (2A/\pi)^{1/4} \times \exp(\imath[k_{iz}(z - z_0) + \mathbf{k}_{i\|}\cdot\mathbf{r}])\exp(-A[z - z_0]^2), \tag{C1}$$

with width $\sigma_z = 1/2\sqrt{A}$ and energy expectation value $E_i = \hbar^2(k_{iz}^2 + \mathbf{k}_{i\|}^2 + A)/2m$. The value of the width parameter A is expressed in terms of the spatial grid Δz(=0.06 Å) as

$$A = 1/[2(\mathrm{NWI}\times\Delta z)^2]. \tag{C2}$$

The initial center of the packet (in angstroms) is set by the condition $z_0 = 1.5 + \mathrm{NZ0}\times\Delta z$. NWI and NZ0 are both integers. The range of z was 1.5–124.32 Å in Paper I (NWI =100), but now for larger values of NWI, it is taken as 1.5–247.2 Å so that the packet can be started far enough from the monolayer that its center is at least $4\sigma_z$ from the interaction region and the potential $V_0(z)$ is a negligible part of the initial energy. The interaction region is considered to start at the classical outer turning point ($\simeq$16 Å for the Xe monolayer) of the shallowest bound state of $V_0(z)$. For NWI=600, this led to a choice z_0=119 Å (NZ0=1960).

The square root of the variance of the energy is

$$\sigma_E \simeq (\hbar^2|k_{iz}|/m)\sqrt{A}. \tag{C3}$$

For $|k_{iz}| \simeq 3.0$ Å^{-1} (a typical value in our examples) and NWI=100, this gives $\sigma_E \simeq 0.4$ meV, comparable to the overall energy resolution of 0.3 meV in recent HAS experiments.

The number of g shells in the Fourier decomposition of the probe-monolayer potential V_s, Eq. (1), is NVG=6. Increasing this parameter to 9 and to 12 had negligible effect. However, decreasing it to 1, in some tests of the coupling schemes, led to pathological behavior (loss of norm) because there are "holes" in the potential energy surface at small z, i.e., the potential energy surface is very corrugated and is poorly represented at small z by the leading Fourier component.

The number of channels is set by including all terms $\mathbf{g}$ coupled to the incident channel and satisfying $(\mathbf{k}_{i\|}+\mathbf{g})^2 \leqslant (2m/\hbar^2)(E_i - E_{\mathrm{cut}})$. In paper I, we used $E_{\mathrm{cut}}=-170$, -250, -430 K for $E_i=8.2$, 16.6, 26.5 meV. For the present work, we have made tests to see that the specular channel strengths and total inelastic strengths have converged to better than 10% and found that $E_{\mathrm{cut}}=-250$ K sufficed for energies of 2–26.5 meV. This surprised us because our reading of the literature[33,34] was that it was expected that we would have to increase $|E_{\mathrm{cut}}|$ as the energy E_i increased. The cutoffs for the SH series at $q=-0.125$ and -0.25 Å^{-1} in this paper are $E_{\mathrm{cut}}=-250$ K for $E_i \leqslant 16.6$ meV and $E_{\mathrm{cut}}=-430$ K for $E_i=26.5$ meV; for the other cases, $E_{\mathrm{cut}}=-170$ K is used for $E_i \leqslant 10$ meV.

For the numerical implementation, a parallel formulation of the computer code was used. Details of that are given in another paper.[35]

[1] B. N. Brockhouse, Rev. Mod. Phys. **67**, 735 (1995).
[2] W. Marshall and S. W. Lovesey, *Theory of Thermal Neutron Scattering* (Oxford University Press, Oxford, 1971).
[3] A. P. Graham, M. F. Bertino, F. Hofmann, J. P. Toennies, and C. Wöll, J. Chem. Phys. **106**, 6194 (1997); **107**, 4445 (1997).
[4] J. Braun, D. Fuhrmann, A. Šiber, B. Gumhalter, and C. Wöll, Phys. Rev. Lett. **80**, 125 (1998).
[5] A. Šiber, B. Gumhalter, J. Braun, A. P. Graham, M. Bertino, J. P. Toennies, D. Fuhrmann, and C. Wöll, Phys. Rev. B **59**, 5898 (1999) and references cited therein.
[6] L. W. Bruch, A. P. Graham, and J. P. Toennies, J. Chem. Phys. **112**, 3314 (2000).
[7] C. Boas, M. Kunat, U. Burghaus, B. Gumhalter, and C. Wöll, Phys. Rev. B **68**, 075403 (2003).
[8] A. P. Graham, Surf. Sci. Rep. **49**, 115 (2003).
[9] L. W. Bruch and F. Y. Hansen, J. Chem. Phys. **122**, 114714 (2005) (denoted as Paper I in the text).
[10] F. Traeger and J. P. Toennies, J. Phys. Chem. B **108**, 14710 (2004) and Ref. 49 therein.
[11] E. R. Bittner and J. C. Light, J. Chem. Phys. **101**, 2446 (1994).
[12] L. Tribe, Chem. Phys. **327**, 468 (2006).
[13] M. I. Hernández, J. Campos-Martínez, S. Miret-Artés, and R. D. Coalson, Phys. Rev. B **49**, 8300 (1994).
[14] It has been suggested that for such corrugated targets, the spectra will be complex and not easy to interpret: H. Jónsson and J. H. Weare, Faraday Discuss. Chem. Soc. **80**, 29 (1985).
[15] C. Carraro and M. W. Cole, Prog. Surf. Sci. **57**, 61 (1998). Using their results, we estimate that the quantum reflection regime would be at $E_i < 50$ neV for ^{4}He/Xe/Pt(111).
[16] Á. Vibók and G. G. Balint-Kurti, J. Phys. Chem. **96**, 8712 (1992).
[17] L. W. Bruch, M. W. Cole, and E. Zaremba, *Physical Adsorption: Forces and Phenomena* (Oxford University Press, Oxford, 1997).
[18] L. W. Bruch, R. D. Diehl, and J. A. Venables, Rev. Mod. Phys. **79**, 1381 (2007).
[19] J. L. Beeby, J. Phys. C **4**, L359 (1971).
[20] B. Gumhalter, Phys. Rep. **351**, 1 (2001).
[21] D. J. Gaspar, A. T. Hanbicki, and S. J. Sibener, J. Chem. Phys. **109**, 6947 (1998); A. Glebov, A. P. Graham, A. Menzel, and J. P. Toennies, *ibid.* **112**, 11011 (2000).
[22] H. Falk, Am. J. Phys. **38**, 858 (1970).
[23] See, for example, Y. Alhassid, R. D. Levine, J. S. Karp, and S. G. Steadman, Phys. Rev. C **20**, 1789 (1979).
[24] Because of the energy spread of the initial wave packet, a part of the norm in channels with small positive Δ may be in true outgoing waves. To quantify this effect for Ψ_0, the projections of the corresponding $\psi_{\mathbf{g}}$ on the bound state wave functions of V_0 are formed and the corresponding total norm is taken to be the bound component.
[25] M. W. Cole and F. Toigo, Phys. Rev. B **23**, 3914 (1981); S. Chung, N. Holter, and M. W. Cole, *ibid.* **31**, 6660 (1985).
[26] C. Schwartz, Phys. Rev. B **34**, 2834 (1986).
[27] S. E. Koonin, *Computational Physics* (Benjamin Cummings, Menlo Park, 1986), Sec. II D
[28] V. Bortolani, A. Franchini, G. Santoro, J. P. Toennies, Ch. Wöll, and G. Zhang, Phys. Rev. B **40**, 3524 (1989).
[29] R. D. Boutchko, Ph.D. thesis, University of Wisconsin-Madison, 2001.
[30] K. Kern, R. David, R. L. Palmer, and G. Comsa, Phys. Rev. Lett. **56**, 620 (1986).
[31] Kinematical focusing is another experimental effect that usually degrades the resolution at positive q. See, e.g., J. P. Toennies, in *Surface Phonons*, Springer Series in Surface Sciences Vol. 21, edited by W. Kress and F. W. de Wette (Springer-Verlag, Berlin, 1991), p. 111.
[32] A. K. Dham, W. J. Meath, A. R. Allnatt, R. A. Aziz, and M. J. Slaman, Chem. Phys. **142**, 173 (1990).
[33] R. A. Aziz, U. Buck, H. Jónsson, J.-C. Ruiz-Suárez, B. Schmidt, G. Scoles, M. J. Slaman, and J. Xu, J. Chem. Phys. **91**, 6477 (1989); **93**, 4492(E) (1990).
[34] K. D. Gibson, C. Cerjan, J. C. Light, and S. J. Sibener, J. Chem. Phys. **88**, 7911 (1988).
[35] F. Y. Hansen, B. Dammann, and L. W. Bruch (unpublished).